Euler-Elastica Variational Model for Pulsed Terahertz 3D Imaging

Yiyao Zhang[1, 2, *], Ke Chen[1], and Shang-Hua Yang[2]

[1] *Centre for Mathematical Imaging Techniques, Department of Mathematical Sciences, University of Liverpool Mathematical Sciences Building, Liverpool, L69 7ZL, United Kingdom*

[2] *Institute of Electronics Engineering, Department of Electrical Engineering, National Tsing Hua University No. 101, Section 2, Kuang-Fu Road, Hsinchu, 30013, Taiwan*

[*] *Yiyao.Zhang@liverpool.ac.uk; yiyaozhang@gapp.nthu.edu.tw*

Abstract: The variational Euler-Elastica model is developed for high-precision terahertz 3D tomographic applications. Our method provides a new approach to mitigate diffraction-limited terahertz reconstructed images with noises and demonstrates the efficient practicality with limited THz datasets.

1. Introduction

Credited to the bio-safe penetrability of terahertz (THz) radiation, 3D nondestructive inspection is one of the primary applications to investigate the interior of visually non-transparent objects. Among different THz 3D imaging methodologies (i.e. THz compressed sensing imaging, THz holographic imaging, THz computed tomographic imaging), THz pulsed imaging based on the THz time-domain spectroscopy (THz-TDS) system plays critical roles in multi-dimensional object information extractions, which is comprised of detailed records by time-resolved THz electric field signals from the interactions between objects under test and broadband THz wave [1–3]. However, the acquisition time of spatial-temporal-spectral data is increasing exponentially due to the nature of the raster scanning, and even the computational time is rising if requiring the image with higher resolution. Additionally, 3D reconstructed quality is strongly influenced by images with diffraction-limited THz beams involving noise sources from the THz-TDS system. Here, we proposed an Euler-Elastica variational model to address the challenges of the efficiency and the quality of undesirable images, paving a new way for high-speed, high-precision THz 3D imaging applications of nondestructive sensing and inspection.

2. Methods and Demonstrations with Quantitative Comparisons

Grounded on the transmission geometry with the schematic diagram of our THz 3D imaging system setup as Fig. 1 depicts, the temporal pulse time-resolved signals for each voxel are recorded by the ASynchronous OPtical Sampling (ASOPS) THz-TDS system (Menlo TERA ASOPS, Menlo Systems). Without the delay stage assemble by mechanisms in conventional THz-TDS systems, the first acceleration of data collection is profited from two asynchronous femtosecond Er-doped fibre lasers with the minor variation of input repetition rates in this ASOPS system so that the data acquisition time is around 5 ms (whereas it would require minutes or even hours in the traditional system) for one THz signal trace with 100 ps time span and the temporal resolution of the dataset is 0.05 ps (2000 sampling points in each voxel) with about 41.7 dB dynamic range from 0.3 THz to 3 THz [2, 3].

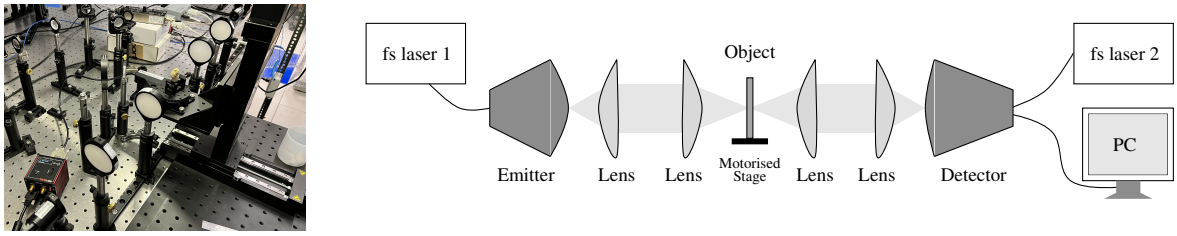

Fig. 1: Schematic diagram of THz 3D Imaging system setup by transmission geometry.

Similar to the previous work (Fig. 2(b)-(c) and (e)-(f)) [4] and based on the diverse reaction between THz wave and samples (Fig. 2(a)), Fourier transform $\mathscr{F}$ is first applied into time-resolved signals $f(t)$ in the time domain for each voxel, and then the phase $\Phi(\omega)$ in the frequency domain to reflect the precise depth can be calculated by $\Phi(\omega) = \tan^{-1}\left(\frac{b}{a}\right)$ where the Fourier amplitude is expressed as $\mathscr{F}(f(t)) = F(\omega) = a(\omega) + ib(\omega) = \int f(t)e^{-2\pi i\omega t}\,\mathrm{d}t$. As Fig. 2(d) illustrated, here the frequency around 1.0010 THz is chosen based on the intensive light-matter interactions between THz wave and various ingredients (fat for peanut kernels and fibre for outer shell). Subsequently, by inverse Radon transform (IRT), the cross sections (slices) can be derived from the input sinograms which are assembled from the projections. To reconstruct a high resolution surface u_ε^* based on low resolution and noisy input surface defined by the interior u_ε^{in} and the exterior u_ε^{ex} with 1 and 0 indicated respectively by the profile function, our proposed variational Euler-Elastica-based model is to minimise the energy

$$u_\varepsilon^* = \mathscr{E}_\varepsilon(u) = \int_\Omega \left(\frac{\varepsilon}{2}|\nabla u|^2 + \frac{1}{\varepsilon}W(u)\right)\mathrm{d}\Omega + \frac{1}{2\varepsilon}\int_\Omega \left(\varepsilon\triangle u - \frac{1}{\varepsilon}W'(u)\right)^2 \mathrm{d}\Omega, \tag{1}$$

which is Γ-convergence approximation to functional energies involving total variations and mean curvatures [5]

$$\Gamma(L^1(\Omega)) - \lim_{\varepsilon\to 0} \mathscr{E}_\varepsilon(u) = \int_0^1 \sqrt{2W(s)}\,\mathrm{d}s \int_{\partial\Omega} (\mathbb{1}_\Omega + |H_{\partial\Omega}|^2)\,\mathrm{d}\mathscr{H}^2, \tag{2}$$

subject to the linear obstacle restriction $u_\varepsilon^{in} \le u \le u_\varepsilon^{ex} \in \Omega \in \mathbb{R}^3$ and the diffuse interface width parameter ε with the double-well potential $W(u) = \frac{1}{2}u^2(1-u)^2$ and its first derivative $W'(u) = u(u-1)(2u-1)$. Next, numerical solution for the Euler-Lagrange equation of (1) is by the projected gradient descent method with a semi-implicit time-stepping scheme in time τ_t where fast Fourier transform will be utilised to speed up the matrix inversion

$$\begin{aligned} u^{d+1} = \left(I_D - \varepsilon\tau_t \triangle + \tau_t\varepsilon\triangle^2\right)^{-1} \Big(u^d - \frac{\tau_t}{\varepsilon}W'(u^{d+1}) + \frac{\tau_t}{\varepsilon}\triangle W'(u^{d+1}) \\ - \frac{\tau_t}{\varepsilon}W''(u^{d+1})\triangle u^{d+1} + \frac{\tau_t}{\varepsilon^3}W'(u^{d+1})W''(u^{d+1})\Big). \end{aligned} \tag{3}$$

Accordingly, to quantify the smoothness of results by Willmore-based formulation and Euler-Elastica-based formulation, the benchmark is devised by computing the standard deviation of Gaussian curvatures (GC) $\sigma_{\text{GC}} := \sigma(\kappa_G)$ and mean curvatures (MC) $\sigma_{\text{MC}} := \sigma(\bar{\kappa})$ from the viewpoint of discrete geometry (more rudiments in [6])

$$\kappa_G(\mathbf{v}_i) = \frac{2\pi - \sum_{k=1}^{\mathbb{N}_{F_{i_R}}} \theta_{i_k}}{\mathscr{A}_{i_R}} \quad \text{and} \quad \bar{\kappa}(\mathbf{v}_i) = \frac{1}{2\mathscr{A}_{i_R}} \sum_{j\in {}_R NV_i} (\cot\alpha_{ij} + \cot\beta_{ij})(\mathbf{v}_j - \mathbf{v}_i) \tag{4}$$

for all vertices in surfaces represented by triangular meshes where $\mathscr{A}_{i_R}$ stands for the appropriately chosen area from the patch within R-ring neighbouring vertices ${}_R NV_i$ around the vertex $\mathbf{v}_i$, θ_{i_k} denotes the angle of the k^{th} face at the vertex $\mathbf{v}_i$, $\mathbb{N}_{F_{i_R}}$ is the total number of faces in the set F_{i_R} around this vertex $\mathbf{v}_i$, as well as α_{ij} and β_{ij} are two angles opposite to the sharing edge in the two triangles. Remark that the lower value of each computing curvatures indicates the better smoothness concerning the variation of curvatures (as illustrations in Fig. 2(f)-(g)).

Eventually, our model with the fast numerical approximation provides a smooth reconstruction (Fig. 2(g)) from only $1/3$ input slices with noise in the low resolution after the selection of crucial features (Fig. 2(e)) not only to improve the quality of 3D reconstruction in the super-resolution but also to reduce scanning time as well as processing time by the efficient algorithm under the low resolution. In other applications like X-ray and magnetic resonance imaging (MRI), our proposed framework can be readily adapted and applied.

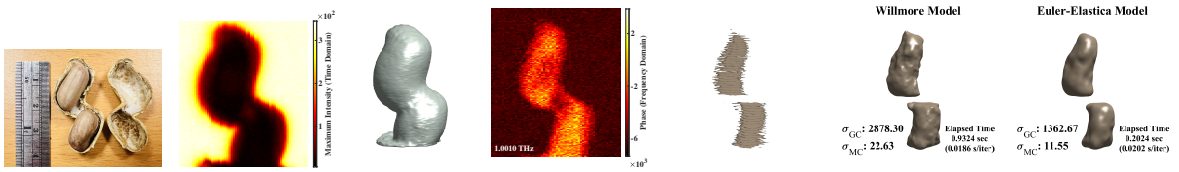

(a) (b) (c) (d) (e) (f) (g)

Fig. 2: Illustrations of (a) the unveiled peanut kernels after scanning by Fig. 1; (b) representative projection of the maximum intensity in the time domain; (c) reconstruction result of peanuts from (b); (d) representative projection of unwrapped phase around 1.0010 THz in the frequency domain; (e) 46 input cross sections (slices) extracted from (d) by IRT; (f) reconstruction result of peanut kernels from (e) by Willmore model [4] with higher computational time (more iterations) and lower smoothness; (g) final reconstruction result of kernels from (e) by new proposed Euler-Elastica model with lower computational time (less iterations) and higher smoothness.

References

1. H. Guerboukha, K. Nallappan, and M. Skorobogatiy, "Toward real-time terahertz imaging," Adv. Opt. Photon, 10, 843–938 (2018).
2. W.-T. Su, Y.-C. Hung, P. Yu, C.-W. Lin and S.-H. Yang, "Physics-guided Terahertz Computational Imaging," IEEE Signal Processing Magazine, 40(1) (2023).
3. Y.-C. Hung, T.-H. Chao, P. Yu, and S.-H. Yang, "Terahertz spatio-temporal deep learning computed tomography," Opt. Express 30, 22523-22537 (2022).
4. Y. Zhang, K. Chen and S.-H. Yang, "Fast Terahertz 3D Super-Resolution Surface Reconstruction by Variational Model from Limited Low-Resolution Sampling," 2022 47th International Conference on Infrared, Millimeter and Terahertz Waves (IRMMW-THz), pp. 1-2 (2022).
5. M. Röger and R. Schätzle, "On a Modified Conjecture of De Giorgi," Mathematische Zeitschrift, 254(4), 675-714 (2006).
6. M. Meyer, M. Desbrun, P. Schröder and A. H. Barr, "Discrete Differential-Geometry Operators for Triangulated 2-Manifolds," in Visualization and Mathematics III, Springer Berlin Heidelberg, 35-57 (2003).